White Rose Research Online

eprints@whiterose.ac.uk
https://eprints.whiterose.ac.uk
Universities of Leeds, Sheffield and York

Deposited via The University of Sheffield.

White Rose Research Online URL for this paper:
https://eprints.whiterose.ac.uk/id/eprint/247222/

Version: Published Version

Article:
Schroeder, J.C., Meegan, J., Rochat, S. et al. (2027) A representative molecular model of the carbon-reinforced PEEK interphase with stochastic vacancy defects. Composites Science and Technology, 287. 111885. ISSN: 0266-3538

https://doi.org/10.1016/j.compscitech.2026.111885

Reuse
This article is distributed under the terms of the Creative Commons Attribution (CC BY) licence. This licence allows you to distribute, remix, tweak, and build upon the work, even commercially, as long as you credit the authors for the original work. More information and the full terms of the licence here:
https://creativecommons.org/licenses/

Takedown
If you consider content in White Rose Research Online to be in breach of UK law, please notify us by emailing eprints@whiterose.ac.uk including the URL of the record and the reason for the withdrawal request.

UNIVERSITY OF LEEDS
University of Sheffield
UNIVERSITY of York

Composites Science and Technology 287 (2027) 111885

Contents lists available at ScienceDirect

Composites Science and Technology

journal homepage: www.elsevier.com/locate/compscitech

A representative molecular model of the carbon-reinforced PEEK interphase with stochastic vacancy defects

Jula C. Schroeder [a,*], Jonathan Meegan [b], Sebastien Rochat [c,d], J. Patrick A. Fairclough [e], Fabrizio Scarpa [a], Ian Hamerton [a]

[a] Bristol Composites Institute, School of Civil, Aerospace, and Design Engineering, University of Bristol, Queen's Building, University Walk, Bristol, BS8 1TR, UK
[b] Syensqo Materials, Abenbury Way, Wrexham Industrial Estate, Wrexham, LL139UZ, UK
[c] School of Chemistry, University of Bristol, Cantock's Close, Bristol, BS8 1TS, UK
[d] School of Engineering Mathematics and Technology (SEMT), University of Bristol, Bristol, BS8 1TW, UK
[e] Department of Mechanical Engineering, University of Sheffield, Sheffield, S1 4BJ, UK

ARTICLE INFO

Dataset link: https://github.com/JulaSchroeder/CF-Surface, Code for graphene sheet generator (Original data)

Keywords:
Carbon fibre
Carbon fibre/PEEK composites
Interphase
Molecular dynamics simulations
Interfacial shear stress

ABSTRACT

Carbon fibre-reinforced polymer composites rely on efficient stress transfer across the fibre–matrix interphase. Yet, real carbon fibre surfaces exhibit nanoscale roughness and vacancy disorder rarely captured in molecular dynamics (MD) models, which typically assume a pristine graphitic surface. This is particularly limiting for thermoplastic matrices such as poly(ether ether ketone) (PEEK), which lack functional groups capable of covalent crosslinking and rely primarily on π-π interactions with the fibre surface, making surface morphology a key determinant of interfacial performance. Here, a stochastic, Perlin-noise-based defect-generation framework is developed to produce graphene-based reinforcements with spatially correlated vacancy defects, motivated by the nanoscale roughness observed via SEM and high-speed AFM characterisation of IM7-GP carbon fibre. The resulting defective reinforcements show progressive degradation in elastic properties, with Young's and shear moduli falling over 80% from pristine to the highest defect threshold, consistent with loss of lattice continuity. Nine stacked configurations were combined with an experimentally validated PEEK matrix to isolate the effect of surface-vacancy morphology on interfacial shear stress (ISS). The defect-free interphase yields composites with an ISS of 63 ± 4 MPa, while low-to-moderate vacancy fractions produce no significant change. In contrast, large, spatially connected vacancy clusters increase ISS by 37–44%, a trend confirmed across two pull-out rates, indicating ISS is controlled by mechanical anchoring of PEEK chains within the vacancy network during pull-out. These results show that the framework generates physically meaningful defect morphologies without an annealing step, and demonstrate that vacancy architecture influences interfacial performance, guiding carbon fibre surface design in thermoplastic composites.

1. Introduction

The aerospace industry is an ever-evolving sector, with each new generation of aircraft demanding improvements in fuel-to-weight efficiency that drive the development of high-performance structural materials [1–4]. Carbon fibre-reinforced polymer (CFRP) composites are well-established in primary aircraft structures, yet the search for more optimised CFRP systems continues [5]. A key route to improving these materials lies in enhancing the interaction between the carbon fibre (CF) reinforcement and the polymer matrix, and computational simulation techniques have emerged as a powerful and efficient means to support this design process [6–9].

Despite the existence of an extensive body of work on interfacial adhesion in CFRP composites, the role of the fibre–matrix interphase in composite mechanical performance remains actively debated, particularly regarding the importance of the contribution of the CF surface [2,10]. CFRP material failure is often traced back to poor interfacial adhesion, but contributions across the macro-, micro-, and nanoscale make this complex region difficult to characterise [11,12]. Numerous experimental approaches have been applied to characterise this region, including atomic force microscopy (AFM), scanning electron microscopy (SEM), and single-fibre pull-out tests [13,14]. While these techniques provide valuable topographical and macroscale mechanical

* Corresponding author.
E-mail addresses: jula.schroeder@bristol.ac.uk (J.C. Schroeder), jonathan.meegan@syensqo.com (J. Meegan), s.rochat@bristol.ac.uk (S. Rochat), p.fairclough@sheffield.ac.uk (J.P.A. Fairclough), f.scarpa@bristol.ac.uk (F. Scarpa), ian.hamerton@bristol.ac.uk (I. Hamerton).

https://doi.org/10.1016/j.compscitech.2026.111885
Received 10 August 2026; Received in revised form 18 September 2026; Accepted 2 October 2026
Available online 10 October 2026
0266-3538/© 2026 The Authors. Published by Elsevier Ltd. This is an open access article under the CC BY license (http://creativecommons.org/licenses/by/4.0/).

data, none can directly reveal how molecules respond at or near the interphase.

Atomistic molecular dynamics (MD) simulations offer a complementary route to address these ambiguities, providing the molecular-level insights needed to inform the optimal design of composite interphases, and crucially, providing an efficient route to screening CFRPs before committing to the full experimental process.

It is important to note that macroscopic phenomena observed during fibre pull-out, such as residual stress, plastic flow, and loading rate effects, cannot be captured using MD [15], or even higher-order atomistic finite element approaches [16–18]. However, MD can qualitatively investigate the molecular-level response at the fibre-matrix interphase by predicting interfacial shear stress (ISS). The ISS is a closely related but distinct quantity to the experimentally measured interfacial shear strength (IFSS), as the IFSS incorporates complex phenomena across many length and time scales that lie beyond the reach of MD, though the two terms are frequently used interchangeably in the literature.

Prior MD studies of CF/epoxy interphases have successfully recovered trends in increased ISS as a function of the architecture of CF-grafted molecules, consistent with experimental single-fibre pull-out data [7,8,19–21]. However, these simulations relied on idealised CF models, where the CF surface is approximated as a three-layer graphitic crystallite [22], a useful simplification that neglects the topographical complexity known to exist on real carbon fibre surfaces. Two broad approaches have since been developed to introduce greater surface complexity into CF models. The first uses reactive force field MD to generate surfaces with physically rich topographic features, including roughness, pores, and non-hexagonal carbon rings, producing structures that more closely resemble those obtained from the carbonisation process but at significant computational cost [23–25]. Vuković and Walsh [24] introduced topographically and topologically rich CF surface models *via* reactive MD annealing, producing surfaces featuring edges, holes, and convergent sheet boundaries characteristic of the carbonisation process, with subsequent work [20] demonstrating that surface roughness and oxidation chemistry each contribute independently to the ISS of CF/epoxy composites.

The second approach removes atoms selectively from graphene sheets [26–29], offering greater computational efficiency and more direct control over defect parameters. Johnston et al. [28] created rectangular voids to represent surface defects and allow mechanical interlocking with the polymer matrix. More recently, Zhang et al. [30] systematically varied vacancy site density across fifty interphase models and demonstrated using a data-driven framework that vacancy density is a primary determinant of interfacial contact density in CF/epoxy composites, while interfacial fracture resistance is determined predominantly by epoxy crosslinking density. Sohail et al. [31] used Fourier decomposition of AFM-measured CF surface profiles to generate surface asperities with sinusoidal graphene surface models, running MD simulations on each component separately and recombining the results to predict ISS for CF/epoxy with reasonable agreement with experimental data. However, the graphene sheets remain structurally intact, modelling surface roughness purely as geometric waviness rather than atomic-scale vacancy defects. The need for automated, tunable defect-generation frameworks has been recognised more broadly, with Garcia et al. [32] introducing a modular tiling strategy to produce hierarchically complex graphene oxide sheet structures for ion transport simulations, with controllable distributions of holes and topological defects. Collectively, these studies highlight that increasing surface complexity in graphene-based models, whether through defect distributions, surface chemistry, or topographic features, consistently yields more physically representative results, motivating the development of approaches that can reproduce the stochastic, multi-scale character of real carbon fibre surfaces.

Additionally, most complex CF models have been tested on thermoset systems, leaving a gap in extending these approaches to thermoplastic polymer systems. Furthermore, no modelling approach has yet examined spatially correlated, pseudo-random vacancy distributions in the classical non-reactive MD style that better characterise representative carbon fibre surfaces than regular geometric patterns or systematic parameter variation.

Extending these interphase models to thermoplastic matrix systems, such as poly(ether ether ketone) (PEEK), introduces additional challenges [33]. PEEK is a promising thermoplastic matrix due to its excellent resistance to harsh environmental conditions, mechanical properties, and processability [34]. However, the relative chemical inertness of the PEEK chains means that, unlike *e.g.* thermoset epoxy, PEEK relies exclusively on van der Waals and π-π interactions with the fibre surface, making surface morphology the dominant variable determining interfacial performance in the absence of covalent crosslinking [35,36]. To date, MD simulations of PEEK interphased with carbon-based reinforcements have employed idealised flat surfaces with no defects or roughness [33,37], and the π-π stacking between the aromatic phenyl groups present in the PEEK and the graphitic surface has been identified as the dominant mechanism driving interfacial interaction energy [37]. SEM and AFM characterisation of IM7-GP carbon fibres conducted in the present work confirms that even fibres known for their smooth surfaces exhibit a coherent nanoscale roughness, motivating the development of surface models that can reproduce this character [38]. The molecular-level interactions dominating the PEEK interface with topographically complex CF surfaces therefore remain unexplored [1,15]. It is worth noting that the term ‘CF’ is commonly used throughout the MD literature to describe idealised graphitic or graphene-based surrogate structures, rather than a structural representation of real, turbostratic carbon fibre. This distinction is adopted in the present work, and ‘CF’ is used hereafter to refer to the modelled graphene-based reinforcement unless explicitly stated otherwise.

In this work, MD is employed to predict the ISS of CF/PEEK interphases and to provide a physical understanding of the role of randomised surface defects in these properties. Perlin noise is a spatially correlated stochastic algorithm originally developed to generate naturalistic, non-repetitive textures in computer graphics [39–42], and has more recently been applied to generate physically realistic rough surfaces in material context, including the modelling of copper surface roughness for laser absorption prediction [43]. Motivated by this, a stochastic defect-generation framework inspired by Perlin noise was introduced to produce spatially correlated vacancy distributions on graphene sheets, which is directly compatible with standard fixed-topology force fields and requires no reactive potentials. A graphical user interface is provided to enable users to generate graphene sheets of varying sizes and defect levels with minimal effort.

2. Methods

2.1. Simulation details

All molecular dynamics (MD) simulations in this work were carried out with the Large-scale Atomic/Molecular Massively Parallel Simulator (LAMMPS) software package [44]. Representative computational performance metrics for the graphene mechanical tests and ISS pull-out simulations are reported in the Supplementary Information (Tables S1 and S2). System topologies and force field parameters were generated using the Enhanced Monte Carlo (EMC) package [45]. The Polymer Consistent Force Field (PCFF) was selected and applied to all atoms (PEEK and composite interphase models), accounting for bond, angle, dihedral, improper, and pairwise interactions. The PCFF force field has proven successful in modelling several polymer systems due to its accurate atomic charge assignment, which is vital for predicting matrix-reinforcement interface properties [46–48]. Non-bonded interactions were described using Lennard-Jones (LJ) and Coulombic potentials with a 10 Å cutoff [7,49], treated within the Particle-Particle Particle-Mesh (PPPM) framework. Further details of the non-bonded interaction parameters are provided in the Supplementary Information. The PEEK

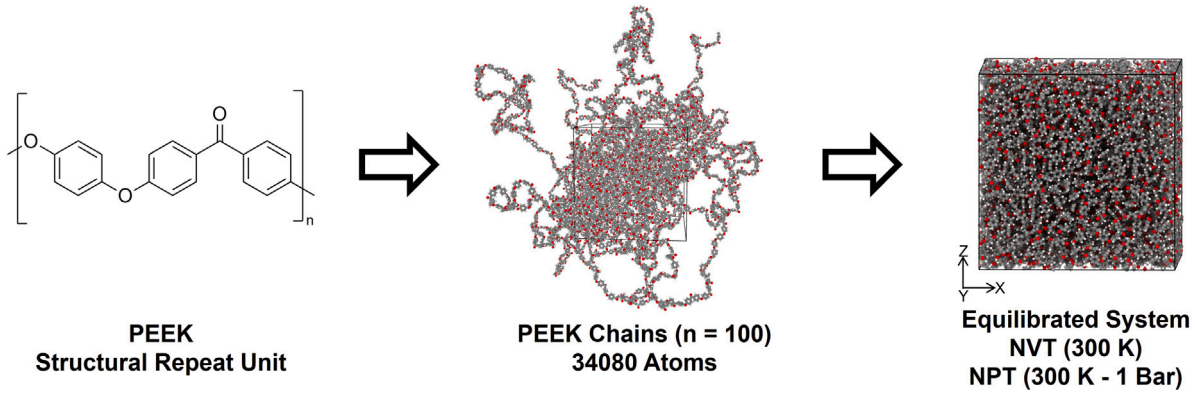


Fig. 1. Repeated structure unit of PEEK, which is extended, replicated, and equilibrated in the canonical (NVT) and isobaric (NPT) ensemble to achieve a densely packed cell.

repeat unit labelled with the corresponding atom types used throughout this work is shown in Figure S1. Additionally, Nosé-Hoover thermostat algorithms were used for all the thermostat and barostat simulations discussed herein [50,51].

All simulations employed periodic boundary conditions in every direction and a consistent time step of 1 fs. Structural analysis and three-dimensional visualisation were performed using the Open Visualisation Tool (OVITO) [52].

2.2. Polymer system

The PEEK molecular model was constructed by extending its structural repeat unit 100 times to form a single polymer chain. Ten such 100-mer chains were then packed into a cubic simulation cell of dimensions 300 × 300 × 300 Å^3, resulting in an amorphous model containing 34 080 atoms, as shown in Fig. 1. PEEK is a widely studied high-performance polymer system due to its favourable thermal and mechanical properties. Hence, molecular modelling studies investigating the thermomechanical properties of PEEK systems have been widely performed [26,37,53].

To ensure the model was well equilibrated and suitable for comparison with experimental data, a multi-stage equilibration protocol was applied. This was particularly important for obtaining reliable estimates of both the glass transition temperature (T_g) and melting temperature (T_m) of PEEK. The equilibration procedure began with energy minimisation, followed by molecular reorientation, after which the system was controlled using the Nosé-Hoover thermostat and barostat to regulate temperature and pressure, respectively.

Minimisation utilised the conjugated gradient (cg) algorithm (Polak–Ribiere) to relax the system fully by using an energy tolerance of 10^{-4}, a force tolerance of 10^{-6}, 1000 maximum iterations and 10 000 maximum force/energy evaluations [54]. Following minimisation, the system was reoriented under constant-volume conditions. To promote efficient reorientation, the system was initially propagated using a Langevin thermostat at 600 K, combined with a microcanonical (NVE) integrator for 250 ps [55]. Subsequently, the simulation was continued for 500 ps under a canonical (NVT) ensemble at 600 K, allowing molecules to fully reorient.

The initial simulation box was intentionally constructed with excess volume to facilitate molecular mobility. To obtain a realistic density, the system was next equilibrated in the isobaric (NPT) ensemble, *i.e.*, at constant pressure. First, the simulation was run at 600 K and an elevated pressure of 100 bar to encourage box contraction. During this stage, the temperature was gradually reduced to 300 K over 50 ps. The system was then further equilibrated at 300 K while the pressure was slowly lowered from 100 bar to 1 bar over 200 ps, resulting in a final average mass density of 1.27 ± 0.05 g cm^{-3}, in good agreement with experimental values (1.30 g cm^{-3}) [3,37,53]. Post-equilibration, a systematic temperature ramp was applied to probe structural and dynamic properties over a broad temperature range. Beginning from 600 K, the system was cooled in increments of 20 K down to 20 K under NPT conditions at 1 bar. At each temperature step, the simulation was run for 200 ps. During these cooling intervals, thermodynamic variables were recorded, and dynamic quantities were computed.

2.3. Carbon reinforcement models

Graphene sheets were generated by defining a hexagonal lattice based on a C–C bond length of 1.396 Å, consistent with the AIREBO potential [56]. Atomic coordinates were constructed by repeating unit cells along the x- and y-directions until the target sheet dimensions of 60 × 60 Å^2 were achieved. Bond connectivity was computed by identifying atom pairs separated by a distance equal to the C–C bond length within a small tolerance of 0.005 Å. The resulting bond list was used to generate a neighbour list for each atom, which was subsequently employed to calculate bond angles by considering unique triplets of connected atoms. The atomic positions were defined in three dimensions, and a small z-displacement was added to each atom to prevent perfect coplanarity.

Graphene defects were introduced using a multi-octave, Perlin-noise-inspired stochastic field [39,40]. The field was constructed by summing successively interpolated Gaussian matrices across multiple scales, producing smoothly varying spatial correlations. Each iteration in the summation corresponds to an octave k, with amplitude A_k proportional to the octave index. The resulting field, $N(x, y)$, is a spatially correlated stochastic map:

$$N(x,y) = \sum_{k=0}^{n-1} A_k \, \mathcal{I}\left(g_k(x,y)\right) \tag{1}$$

where $g_k(x, y)$ is the interpolated random field at octave k and $\mathcal{I}$ denotes spline interpolation. The noise field was then normalised as:

$$N_{\text{norm}}(x,y) = \frac{N(x,y) - \min(N)}{\max(N) - \min(N)} \tag{2}$$

to ensure all values lay within $[0, 1]$ prior to thresholding. The normalised field was interpolated on to the atomic positions (x_i, y_i) to assign a defect probability p_i to each atom:

$$p_i = N_{\text{norm}}(x_i, y_i) \tag{3}$$

Atoms were deleted if p_i exceeded a threshold T, which was varied systematically to generate different vacancy fractions. The resulting vacancy fraction is defined as:

$$\phi_{\text{vac}} = \frac{1}{N} \sum_{i=1}^{N} H(p_i - T) \tag{4}$$

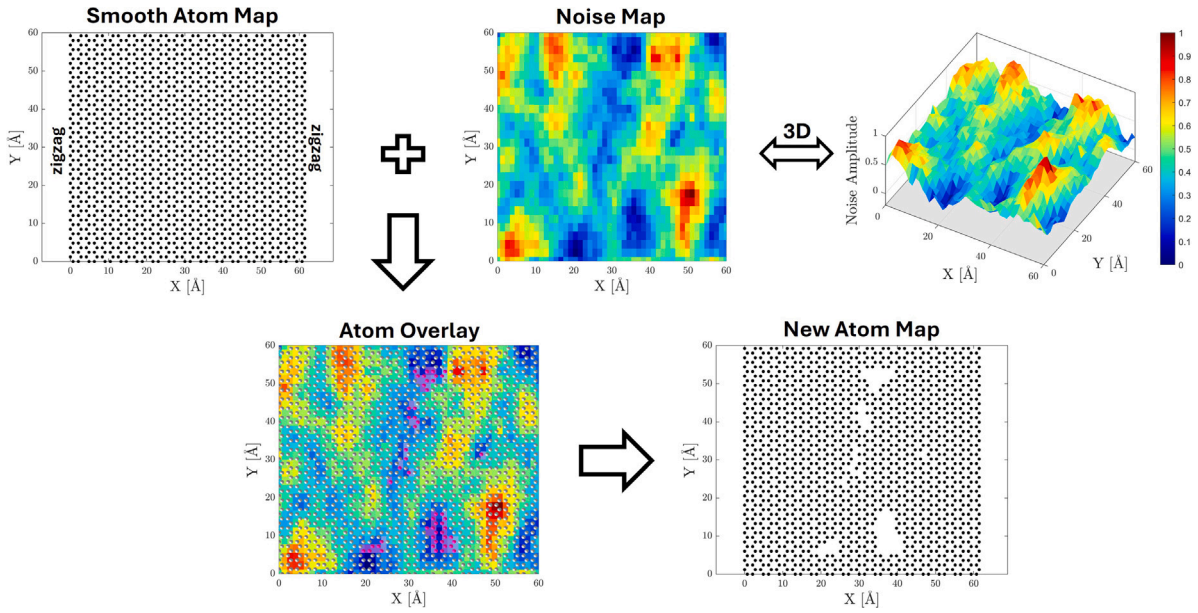


Fig. 2. Schematic of the Perlin-noise defect generation procedure. The pristine graphene atom map (top left) is combined with the 2D noise amplitude field $N_{\mathrm{norm}}(x, y)$ (top centre) and its equivalent 3D surface representation (top right). The atomic positions are overlaid on the noise field (bottom left), where highlighted atoms (pink) exceed the deletion threshold T and are removed, yielding the final defective graphene sheet (bottom right).

where $H(\cdot)$ is the Heaviside step function and N is the number of atoms prior to deletion. Four threshold levels were investigated, denoted P1, P3, P5, and P7, corresponding to progressively higher vacancy fractions. The spatial character of the resulting defect distributions is illustrated in Fig. 2. The defect-generation procedure overlays the normalised noise field on the atomic positions, highlighting and removing atoms with assigned probability p_i exceeding the threshold T, as shown in Fig. 2. This produces spatially correlated vacancy clusters whose size and connectivity increase with T: at low thresholds (P1), the vacancies manifest as isolated vacancy defects and short linear clusters, while at higher thresholds (P5, P7) extended vacancy networks develop that span a significant fraction of the sheet area, with P7 approaching a percolating void regime in which the sheet loses structural continuity. Five independent realisations were generated at each threshold to ensure statistically robust mechanical property estimates, as shown in Fig. 3. The mean vacancy fraction per threshold level relative to the smooth graphene sheet is described in Table S3.

Uniaxial tensile and in-plane shear deformations were applied to each sheet (using the AIREBO potential) to extract the elastic constants of the defective graphene models. Uniaxial tension was applied separately along the zigzag and armchair orientations using a constant engineering strain rate of 1×10^9 s^{-1} under the *NVT* ensemble at 300 K [57]. The Young's moduli E_{11} and E_{22} were extracted by fitting a linear function to the stress–strain response within the elastic regime ($\epsilon \leq 0.05$), following:

$$E = \left.\frac{\Delta\sigma}{\Delta\varepsilon}\right|_{\varepsilon \leq 0.05} \tag{5}$$

The Poisson's ratios ν_{ij} were computed from the ratio of average transverse to axial engineering strains (across the whole RVE cell) recorded during each uniaxial simulation, evaluated as:

$$\nu_{ij} = -\left.\frac{\epsilon_j}{\epsilon_i}\right|_{\epsilon_i = 0.03} \qquad i, j = 1, 2 \quad i \neq j \tag{6}$$

where the engineering strains were computed from the time-evolving simulation box dimensions L_i. In-plane shear simulations were performed using the G_{12} deformation method, from which the shear modulus was determined by fitting the initial linear portion of the shear stress-shear strain response over the same strain range.

2.4. Modelling the CF/PEEK composite interphase

The nanocomposite sandwich model was constructed by first stacking multiple graphene sheets (3 or 5) along the z-axis with an interlayer spacing of 3.4 Å, consistent with the graphitic interlayer distance [58]. The graphene sheet configurations used to represent the CF surface in the composite interphase system are summarised in Table 1 and shown in Fig. 4, where each composite sample is constructed by stacking individual graphene sheets in the sequence specified (dimensions and vacancy fractions given in Table S4). The graphene stacks were then positioned between two equilibrated PEEK blocks, with the final assembled systems containing approximately 196,000 atoms, with the PCFF force field applied to all components (reported in Tables S5 and S6).

The assembled systems were energy minimised, followed by a short *NVT* reorientation run at 300 K using a Langevin thermostat for 5 ps. The PEEK matrix was then densified toward a target density of 1.30 g cm^{-3} by applying affine box deformation under *NVT* conditions at 300 K with a Nosé-Hoover thermostat, while the graphene sheets were restrained in z *via* a harmonic spring fix ($k = 0.1$ kcal mol^{-1} Å^{-2}) to maintain their position during compaction. Once the target density was reached, a 40 ps relaxation run was performed to allow the system to reach equilibrium at 300 K and 1 atm. The interaction energy (IE) and radial distribution function (RDF) between each PEEK atom type and the graphene carbon atoms were computed throughout the simulation to monitor structural equilibration at the interphase.

The ISS was determined *via* graphene substrate displacement simulations. Prior to pull-out, the relaxed sandwich system was re-minimised and equilibrated under *NVT* conditions at 300 K for 50 ps. The graphene sheets were then displaced along the x-axis using a linear move fix over a total pull distance of 40 Å, consistent with literature [8,9,20]. All remaining atoms were thermostatted using a Langevin thermostat at 300 K, combined with an *NVE* integrator, so that only the graphene carbon atoms were driven, while all polymer atoms remained free to respond to the evolving interphase.

The ISS was calculated from the work associated with the substrate displacement, obtained from the change in total potential energy, W, at a fixed displacement $l = 40$ Å, following established approaches [9,

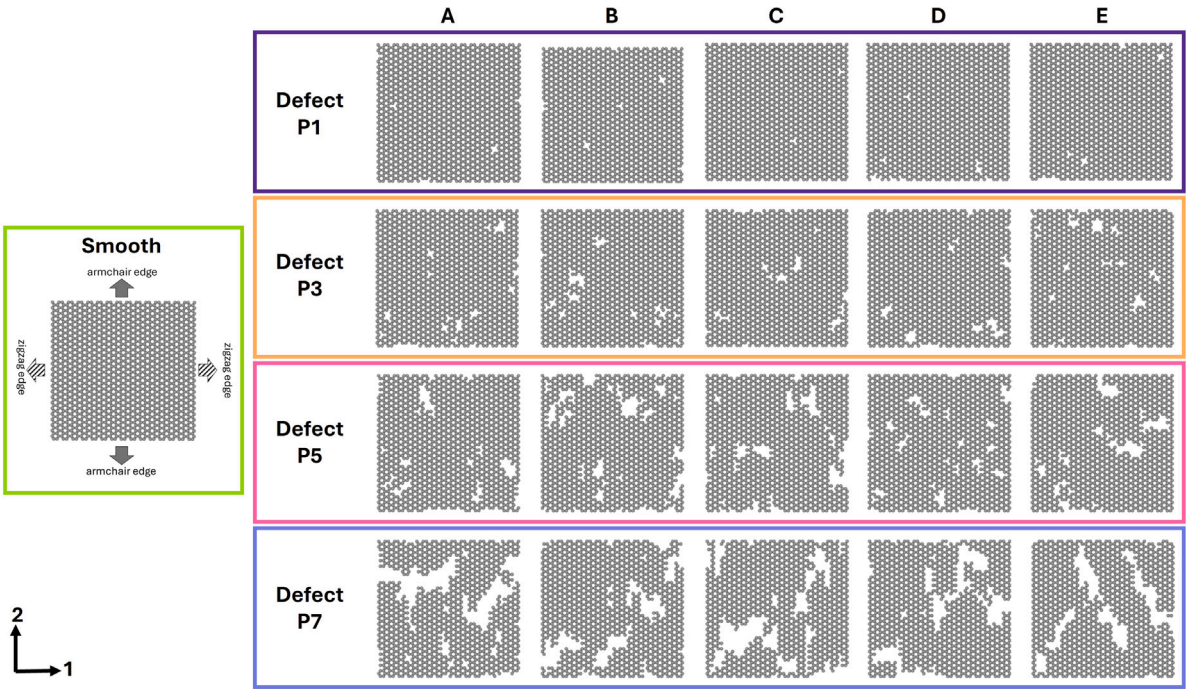


Fig. 3. Representative graphene sheets generated at noise defect thresholds P1, P3, P5 and P7, showing five independent realisations (A–E) at each level. The smooth (pristine) sheet is shown for reference. Mean vacancy fractions ϕ_{vac}: P1 0.5 ± 0.2%, P3 2.7 ± 0.3%, P5 6.8 ± 1.6%, P7 15.2 ± 2.4%.

Table 1
Summary of graphene sheet configurations used in the CF/PEEK composite models. For each sample, the total number of carbon atoms, perimeter edge atoms, internal sp^2 atoms, vacancy-induced sp atoms, missing internal atoms relative to the smooth reference, and vacancy fractions (ϕ_{vac}) are reported.

Sample	Sequence[a]	Layers	Total C	Edge C	sp^2 C	sp C	Missing	ϕ_{vac} [%]
Smooth	s-s-s	3	26 100	792	25 308	0	0	0.00
C1	a-s-a	3	25 670	792	24 246	632	430	1.70
C2	a-b-a	3	25 230	792	23 349	1089	870	3.44
C3	d-d-d	3	24 078	792	21 477	1809	2022	7.99
C4	c-c-c	3	24 393	792	22 317	1284	1707	6.74
C5	c-b-c	3	24 522	792	22 417	1313	1578	6.24
C6	f-s-f	3	20 028	792	18 388	848	6072	23.99
C7	f-e-f	3	18 803	792	16 828	1183	7297	28.83
C8	f-e-s-e-f	5	34 978	1320	32 140	1518	8522	20.20

[a] Sequence labels denote the stacking order of the individual graphene sheets shown in Fig. 4 (smooth: 's'; defective: 'a'–'f'), listed in the order the layers appear through the thickness of the stack (e.g. 'a-s-a' = defective-smooth-defective).

20,59]:

$$\tau = \frac{W}{2\,l\,L_x\,L_y} \tag{7}$$

where L_x and L_y are the in-plane x and y dimensions of the graphene sheets, and the factor of two accounts for the two PEEK-graphene interphases present in the sandwich geometry. The potential energy was recorded at each time step and smoothed with a uniform linear filter. Simulations were performed at two pull velocities (0.5 Å ps^{-1} and 1.25 Å ps^{-1}) to assess rate sensitivity, with five independent PEEK realisations per defect configuration for statistically robust ISS estimates. As noted in prior simulation studies [24], these velocities are several orders of magnitude higher than experimentally accessible rates; therefore, this work focuses on relative trends in ISS across vacancy configurations. Furthermore, the assembled CF/PEEK systems and their vacancy fractions are not intended to reproduce the exact in-plane vacancy fraction, vacancy size, or spatial cluster distribution of the IM7-GP fibre surface. The calculated surface roughness and characteristic spatial correlation length (λ_c) of the MD models, obtained directly from the pull-out configuration files, provide quantitative descriptors of the generated surfaces (Table S8), but the AFM data cannot directly determine atomic-scale vacancy features. Instead, the defect configurations provide controlled atomistic representations of increasing vacancy content and connectivity, allowing the effect of vacancy morphology on interfacial stress transfer to be isolated.

3. Experimental

3.1. Materials

PEEK 450G was obtained from Victrex (Wrexham, UK). Carbon fibre (IM7-GP, 12 K, nominal diameter 5.2 μm) was obtained from Hexcel Composites (Duxford, UK).

3.2. Thermal analysis

Differential scanning calorimetry (DSC) measurements of the PEEK samples were conducted using a Discovery DSC 2500 instrument (TA Instruments, Delaware, USA) following a heat-cool-heat analysis from −50 °C to 380 °C at a heating and cooling rate of 10 °C min^{-1}. The analysis was conducted under inert nitrogen gas (60 ml min^{-1}). The

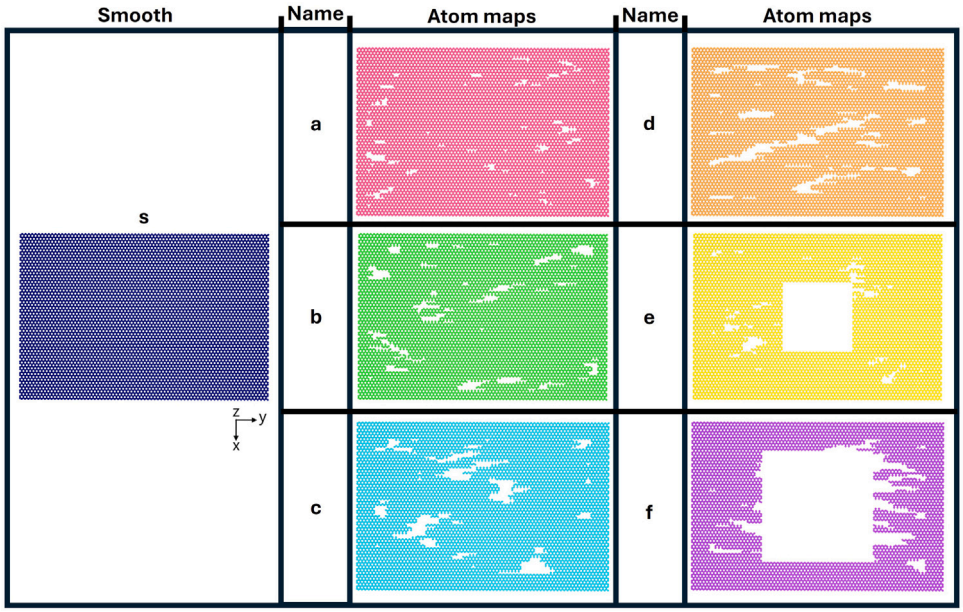


Fig. 4. Graphene sheet generation for modelling representative CF/PEEK composite systems. Mean dimensions of sheets are 120.06 Å × 180.14 Å (Table S4). Individual sheets are labelled s (smooth, non-defective $\phi_{vac} = 0\%$) and a–f (defective, ϕ_{vac} = 2.55, 5.22, 6.75, 7.99, 14.52, and 35.99%, respectively). Composite stacking sequences and resulting vacancy fractions are given in Table 1.

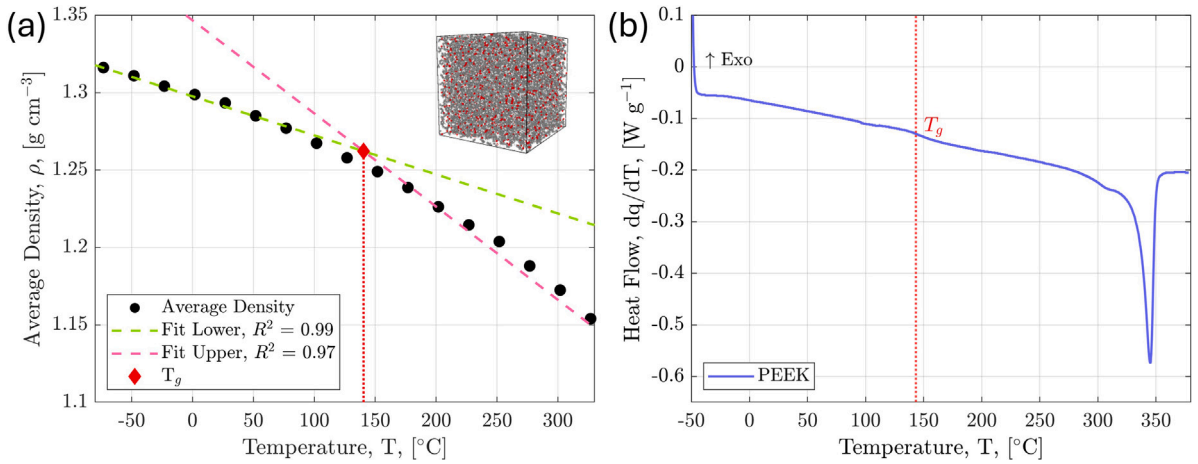


Fig. 5. Thermal validation of the PEEK matrix: (a) average mass density as a function of temperature from MD simulation, with bilinear fits used to determine T_g (red diamond); (b) second heat DSC curve of neat PEEK.

glass transition temperature (T_g) and the melting temperature (T_m) were determined from three repeated measurements.

3.3. Characterisation of carbon fibre morphology

The surface morphology of the IM7-GP carbon fibre was characterised by scanning electron microscopy (SEM) (JEOL JSM-IT300) at 15 kV and high-speed atomic force microscopy (HS-AFM). The contact mode HS-AFM instrument was developed at the University of Bristol and Bristol Nano Dynamics Ltd. (UK). Roughness measurements were averaged across three fibres, and topographic data were analysed using Gwyddion SPM data-processing software [60].

4. Results and discussion

4.1. Polymer validation

Before a representative CF/PEEK interphase model can be constructed, the polymer matrix must be validated against experimental data. PEEK was treated as an amorphous polymer (it is accepted that it is a semi-crystalline polymer in reality), and its thermal properties were characterised *via* both MD simulation and DSC measurements. While semicrystalline PEEK would more closely represent the material in service, the amorphous model was adopted here due to the computational cost of constructing and equilibrating a crystalline unit cell at the scale required for the composite interphase simulations [61]. Kashmari et al. [53] extended this approach to semicrystalline PEEK to determine thermomechanical properties, providing a natural starting point for incorporating crystallinity in future work. From the bilinear regression of the MD density-temperature curve in Fig. 5(a), the T_g was predicted to be 140.45 ± 10.3 °C, in good agreement with the experimental value of 144.25 ± 1.09 °C determined from the second heat DSC curve (Fig. 5(b)), which also yields a T_m of 345.15 ± 0.21 °C.

Temperature fluctuations are expected in MD simulations during the heating ramp, owing to the dynamic nature of atomistic systems. To reduce these fluctuations, sufficient equilibration at each temperature step during the cooling cycle is essential, as highlighted in previous MD studies [62,63].

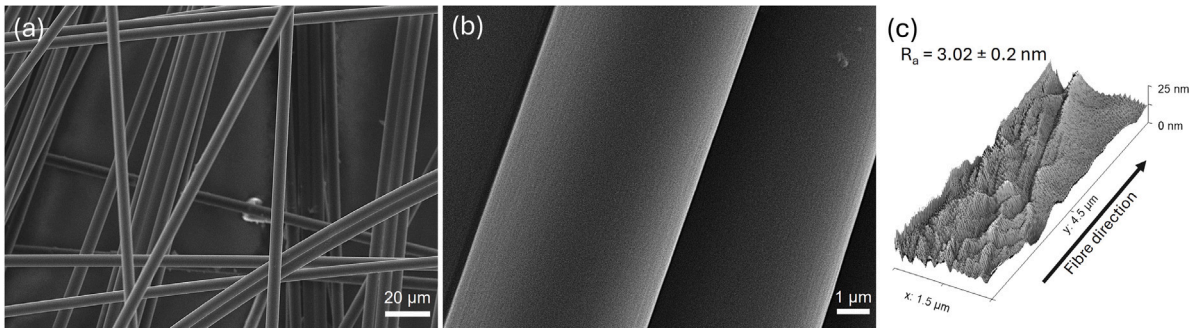


Fig. 6. SEM images of IM7 fibres: (a) pure fibre strands, (b) expanded image of the surface of an IM7 carbon fibre, and (c) the representative AFM roughness analysis of the fibre.

4.2. Mechanical properties of defective graphene-based reinforcements

Carbon fibres are frequently represented in MD simulations as stacks of pristine graphene sheets, yet real carbon fibres exhibit considerably more complex surface morphology than ideal hexagonal lattices. To investigate this, the surface of IM7-GP carbon fibre, a fibre known for its high strength and nominally smooth character, was characterised using SEM and HS-AFM. As shown in Fig. 6, surface roughness is not immediately apparent from SEM alone but becomes clearly visible under AFM, yielding an arithmetic mean roughness (R_a) value of 3.02 ± 0.2 nm along the fibre direction. Translating such surface imperfections into MD models is therefore important to obtain a more physically representative CF/PEEK interphase [31]. However, topographic roughness alone does not capture the full complexity of real carbon fibre surfaces. Vacancy defects intrinsic to graphitic systems represent a further structural dimension that AFM cannot resolve. Characterisation of such defects has been demonstrated by Rothe et al. [64] using scanning tunnelling microscopy (STM) topographies combined with AFM, revealing that graphitic surfaces possess structural disorder well beyond what is typically represented in MD models [65]. Computational studies using the atomic finite element method (AFEM) have confirmed that such vacancy defects significantly degrade the elastic properties of graphene. At a 10% defect concentration, Young's modulus and shear modulus are reduced by approximately 60% and 63%, respectively, in single-layer graphene [66].

Before the CF/PEEK interfacial properties can be analysed, the graphene-based reinforcements used to represent the carbon fibre surface must also be validated, as this step is often omitted in the literature despite being as critical as the polymer matrix validation. Prior to investigating the defective systems, the smooth graphene model (no defects) was validated against established experimental values. The pristine sheet yielded $E_{11} = 954 \pm 18$ GPa and $E_{22} = 839 \pm 24$ GPa along the zigzag and armchair directions, respectively, and a shear modulus of $G_{12} = 270 \pm 5$ GPa, in good agreement with the experimentally reported values of 1 ± 0.10 TPa (Young's modulus) [67] and 270 ± 30 GPa (shear modulus) [68]. This agreement confirms that the graphene-based reinforcements modelled herein are suitable as a carbon fibre surface surrogate, consistent with established practice in MD simulations [9].

Having validated the smooth graphene model, the effect of introducing vacancy defects at increasing thresholds was investigated. Perlin noise, originally developed to generate naturalistic textures in computer graphics, such as terrain surfaces [39], was adopted here because it produces spatially correlated vacancy clusters that better reflect the localised damage character of real carbon fibre surfaces than does uniform atom deletion. The stress–strain curves under uniaxial tension are shown in Fig. 7(a). All systems exhibit a linear-elastic regime at low strains ($\varepsilon < 0.05$), followed by nonlinear hardening prior to brittle fracture. The smooth graphene sheet sustains the highest fracture strain, reaching failure at an ultimate tensile strength of 108 GPa at $\varepsilon_{22} \approx 0.21$ in the armchair direction and 91 GPa at $\varepsilon_{11} \approx 0.14$ in the zigzag direction, consistent with the known directional anisotropy of graphene fracture, whereby the armchair direction exhibits greater ductility than the zigzag due to differences in bond orientation relative to the loading axis [57]. With increasing defect threshold, both the ultimate tensile strength and fracture strain decrease, from 67.6 ± 6.5 GPa at $\varepsilon_{11} \approx 0.088 \pm 0.01$ for P1 (zigzag) down to 10.2 ± 7.5 GPa at $\varepsilon_{11} \approx 0.061 \pm 0.05$ for P7 (fracture strain values and UTS are reported in Table S7). The P1 and P3 configurations retain a well-defined linear-elastic regime and a single abrupt fracture event, whereas P5 and P7 exhibit increasingly progressive stress drops prior to final failure, reflecting the formation of distributed damage around the larger vacancy clusters and edge defects.

Table 2
Elastic constants of pristine and defective graphene sheets from MD simulations, compared with experimental reference values. All configurations were run across the five realisations (A–E) (Table S3), with uncertainties representing the standard deviation across the five realisations. Dashes for P5 and P7 indicate cases where reliable extraction was not possible due to excessive scatter.

Configuration	E_{11} [GPa]	E_{22} [GPa]	G_{12} [GPa]	ν_{12}	ν_{21}
Experimental	1000 ± 100 [67]		270 ± 30 [68]	0.165 [69]	
Smooth	954 ± 18	839 ± 24	270 ± 5	0.12 ± 0.02	0.24 ± 0.02
P1	869 ± 28	786 ± 38	236 ± 16	0.12 ± 0.03	0.20 ± 0.02
P3	696 ± 31	663 ± 17	186 ± 7	0.19 ± 0.02	0.24 ± 0.07
P5	453 ± 78	404 ± 112	100 ± 36	–	–
P7	162 ± 74	187 ± 95	54 ± 26	–	–

The Young's moduli are presented in Fig. 7(b) and Table 2. A clear reduction in both E_{11} and E_{22} is observed with increasing defect threshold, consistent with the linear degradation trend reported by Jafari et al. [66] using AFEM across comparable defect concentrations. The P1 configuration retains approximately 90% of the smooth sheet stiffness, whereas at P5, corresponding to a vacancy fraction of 6.76 ± 1.57%, the moduli are reduced by 53%. By P7, the moduli have fallen to 162 ± 74 GPa and 187 ± 95 GPa in the zigzag and armchair directions, respectively, representing reductions of over 80% relative to the pristine case. The larger standard deviations at P5 and P7 reflect the stochastic nature of the defect generation: at high vacancy fractions, different realisations at the same threshold produce vacancy distributions with varying degrees of spatial connectivity, leading to significant variability in the onset of fracture.

The in-plane shear stress–strain response is shown in Fig. 7(c). The smooth sheet exhibits a continuously hardening response throughout the applied strain range. The defective sheets show a progressive reduction in initial shear stiffness with increasing vacancy fraction and, at higher levels (P3 and above), exhibit a distinct load drop indicative of localised shear fracture propagating through the vacancy-rich regions. The shear moduli G_{12}, presented in Fig. 7(d), decrease from 270 GPa for the smooth sheet to 54 ± 26 GPa for P7, mirroring the trend in

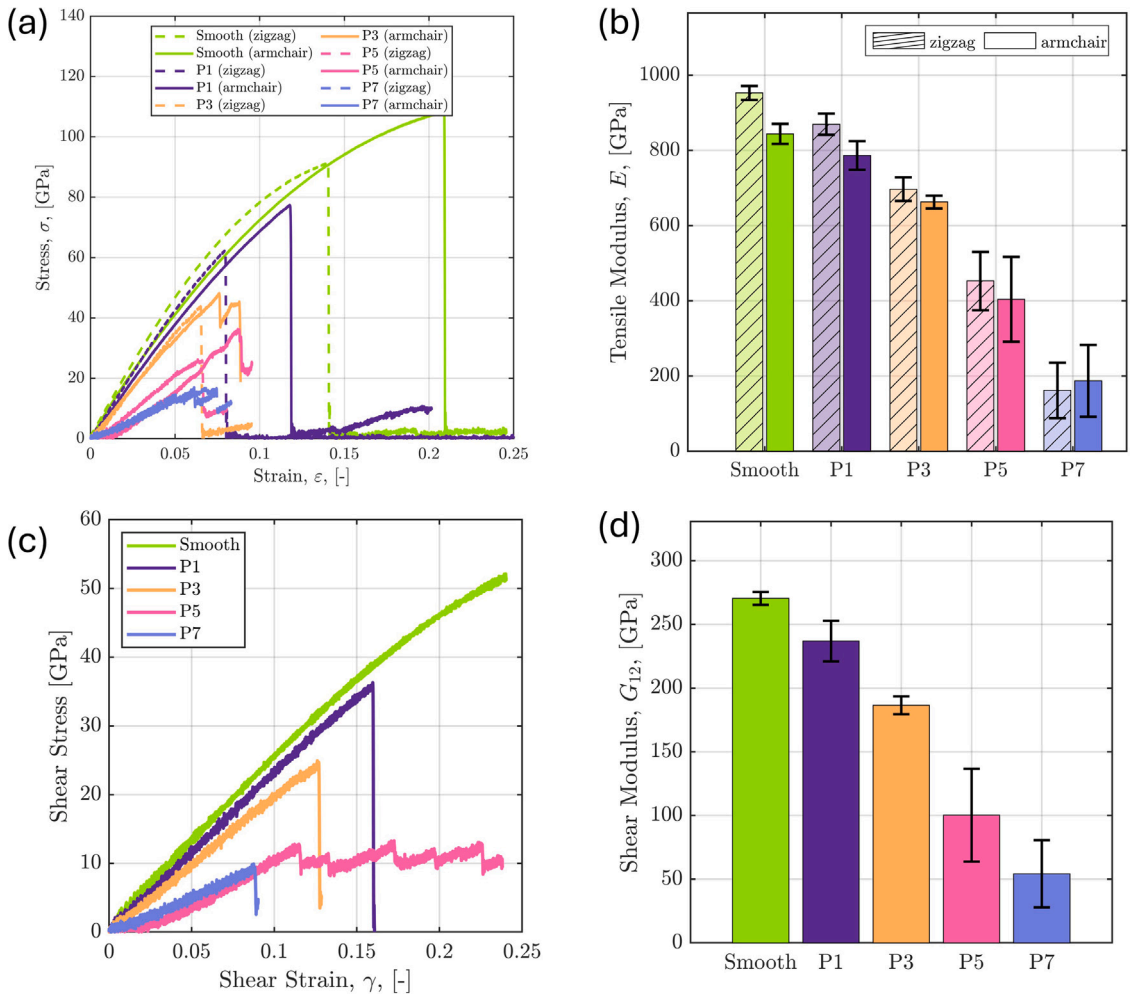


Fig. 7. Mechanical properties of pristine and defective graphene sheets under uniaxial tension and in-plane shear. (a) Stress–strain curves along the zigzag and armchair directions for the smooth sheet and each defect threshold (P1, P3, P5, P7). (b) Tensile modulus, E_{11} (zigzag) and E_{22} (armchair), as a function of defect threshold. (c) Shear stress-shear strain response for each configuration. (d) Shear modulus, G_{12}, as a function of defect threshold. All configurations, including the smooth sheet, were run across the five realisations (A–E) shown in Fig. 3, with error bars representing one standard deviation.

the tensile moduli and confirming that vacancy defects degrade all components of the in-plane elastic stiffness tensor consistently.

The Poisson's ratios ν_{12} and ν_{21} were extracted reliably for the smooth, P1, and P3 configurations, yielding values in the range 0.12–0.24, broadly consistent with the experimental Poisson's ratio for graphene of approximately 0.165 [69,70]. For P5 and P7, the scatter in the lateral strain response prevented meaningful extraction, a consequence of highly heterogeneous vacancy distributions that produce large-scale deformation fields. Notably, Jafari et al. [66] report that Poisson's ratio is particularly sensitive to vacancy defects, increasing substantially with defect concentration; the inability to extract reliable values at P5 and P7 in the present MD simulations is consistent with this heightened sensitivity at elevated vacancy fractions.

4.3. ISS analyses and matrix response

Herein, the analysis of the composite CF/PEEK models is presented, combining the validated PEEK matrix with the graphene stacks described in Section 2 as a surrogate for the carbon fibre surface. The sandwich geometry is illustrated in Fig. 8(a). The surface morphology of the CF configurations was quantified using the arithmetic mean roughness (R_a), root-mean-square roughness (R_q), and characteristic in-plane spatial correlation length (λ_c) (Table S8). Prior to the pull-out simulations, the interaction energy (IE, defined as $\Delta E = E_{\text{total}} - E_{\text{CF}} - E_{\text{PEEK}}$) between the PEEK matrix and each CF configuration was computed to characterise the initial interfacial adhesion, as shown in Fig. 8(b). More negative IEs indicate stronger PEEK-CF attraction.

The smooth configuration yields the strongest IE ($-10,860 \pm 81$ kcal mol^{-1}), consistent with the pristine plane providing the maximum available π-conjugated surface area for van der Waals and π-π interactions with the PEEK aromatic rings. PEEK has been shown to interact strongly with graphitic systems [37], primarily through aromatic π-π stacking between the phenyl groups of the PEEK backbone and the graphene basal plane [7,35]. Configurations with low-to-moderate vacancy fractions (C1, C2, C4, C5) retain interaction energies within approximately 10% of the smooth baseline, suggesting that sparse vacancy distributions do not significantly disrupt the interfacial contact area. By contrast, configurations C3, C6, and C8 show more pronounced reductions, reflecting the larger or more spatially connected vacancy clusters in these arrangements. C7, which features a large centralised void representative of severe localised damage such as that induced by gamma-ray irradiation [26], exhibits the lowest IE (-7891 ± 15 kcal mol^{-1}), consistent with the reduction in available contact area. Notably, configurations incorporating stepped or layered vacancy arrangements (C6, C8) allow PEEK chains to penetrate into the vacancy regions and interact with the graphene edges in the z-direction, potentially enabling mechanical interlocking that may partially compensate for the reduced van der Waals contact area during pull-out.

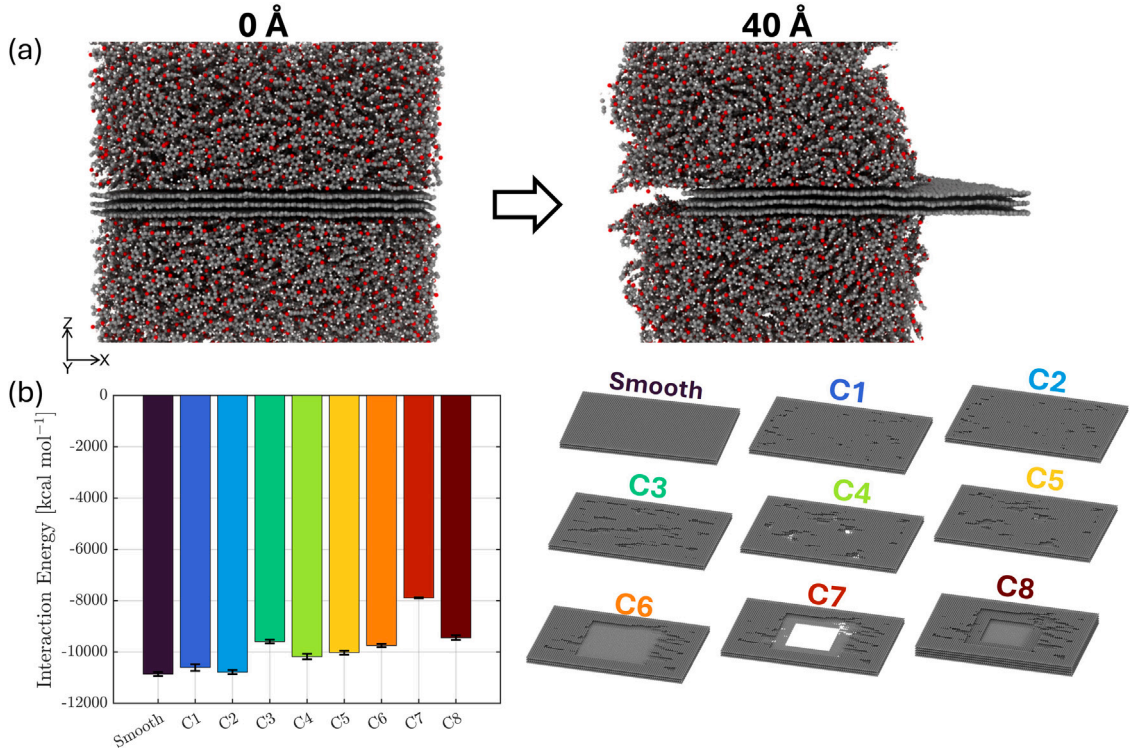


Fig. 8. CF/PEEK interfacial model and interaction energy analysis. (a) Representative snapshots of the sandwich model at 0 Å and 40 Å graphene displacement, showing PEEK chains being dragged longitudinally during pull-out. (b) Mean IE between the PEEK matrix and graphene stack prior to pull-out for each configuration, with error bars representing one standard deviation across five independent realisations.

To characterise the response of the polymer matrix to CF displacement, the PEEK displacement density was computed by binning the total displacement of matrix atoms, resolved into components longitudinal and transverse to the pull-out direction, as a function of the relative z coordinate spanning the two PEEK blocks and the intervening CF, as shown in Fig. 9(a) and (b).

All configurations show a pronounced peak in longitudinal displacement density immediately adjacent to the CF (Fig. 9(a)), consistent with polymer chains in direct contact with the CF surface being carried along during pull-out. The smooth sheet and low-to-moderate defect configurations (C1–C5, $\phi_{vac} = 1.7\% - 8.0\%$; Table 1) show comparable, relatively narrow interfacial peaks, whereas C6, C7 and C8 ($\phi_{vac} = 20 - 29\%$) show substantially taller and broader peaks extending further into the matrix on the trailing side of the graphene stack. This broadening indicates that a larger volume of PEEK is displaced at high vacancy fractions, consistent with vacancy clusters and open voids that permit PEEK chain segments to penetrate the sheet plane and become anchored within the defect structure, rather than sliding freely past an intact surface. The transverse displacement density (Fig. 9(b)) follows a similar pattern but is more sensitive to defect level: C7 and C8 exhibit transverse peaks roughly double those of the remaining configurations, indicating that matrix chains anchored within the larger vacancy features are displaced substantially off-axis as the CF pulls past them — direct evidence of mechanical interlocking.

This chain anchoring is directly reflected in the potential energy and shear force responses (Fig. 9(c,d)). ΔPE increases approximately linearly with displacement for all configurations, but C6, C7 and C8 diverge above the remaining samples from around $\Delta x \approx 10$ Å onward, reaching 30 – 45% higher ΔPE than the smooth baseline by $\Delta x = 40$ Å. The shear force profiles (Fig. 9(d)) show an initial elastic loading peak within the first ~3 Å of displacement, followed by a drop to a steady-state sliding regime, with two groups emerging clearly: C6–C8 sustain peak forces of 730–840 kcal mol^{-1} Å^{-1} and steady-state forces of roughly 450–600 kcal mol^{-1} Å^{-1}, compared with peak forces below 600 and steady-state forces below 250 kcal mol^{-1} Å^{-1} for the smooth sheet and C1–C5. The persistence of elevated shear force well beyond the initial loading peak is consistent with repeated engagement and release of PEEK segments from the vacancy network during pull-out, rather than a single interfacial detachment event. Patil et al. [26] showed a similar trend in which friction forces increase as the morphology of the graphitic system changes, and it has been suggested more broadly that shear force improves significantly upon introducing defects and functional groups [8].

The ISS values obtained from these simulations (0.5 Å ps^{-1}, computed from ΔPE per Eq. (7)) are summarised in Fig. 10(a). Unlike the monotonic degradation of the in-plane elastic constants reported in Section 4.2, the ISS response to vacancy defects was non-monotonic. The smooth interphase yielded an ISS of 62.9 ± 3.8 MPa, and configurations C1–C5 produced ISS values statistically indistinguishable from this baseline (60.4 ± 4.0 to 71.7 ± 4.0 MPa; one-way ANOVA against the smooth control, $p > 0.10$ for every comparison in this range). The full ISS results and ANOVA analysis can be found in Table S9. Whilst direct quantitative comparison with experiment is precluded by the orders-of-magnitude difference in pull-out velocity, the predicted ISS for the smooth and low-vacancy configurations falls within a factor of two of experimentally reported CF/PEEK interfacial shear strengths of 43.2 ± 5.9 MPa [15] and comparable values reported elsewhere [71–73], broadly consistent with the expected rate-dependent overestimation inherent to MD pull-out simulations. At higher vacancy fractions, ISS rose sharply: C6, C7 and C8 ($\phi_{vac} = 24.0\%$, 28.8%, and 20.2% respectively) gave 86.2 ± 3.1, 90.6 ± 8.7, and 87.5 ± 1.5 MPa, each significantly greater than the smooth baseline ($p < 0.001$), an increase of 37–44% relative to the pristine interphase. This magnitude of enhancement is qualitatively consistent with experimentally reported increases in fibre-matrix interfacial strength following carbon-fibre surface modification, including CF/PEEK systems [74,75] and irradiation-induced surface modification of carbon fibres in other polymer matrices [76–78]. C6–C8 showed no significant separation from one another, and a

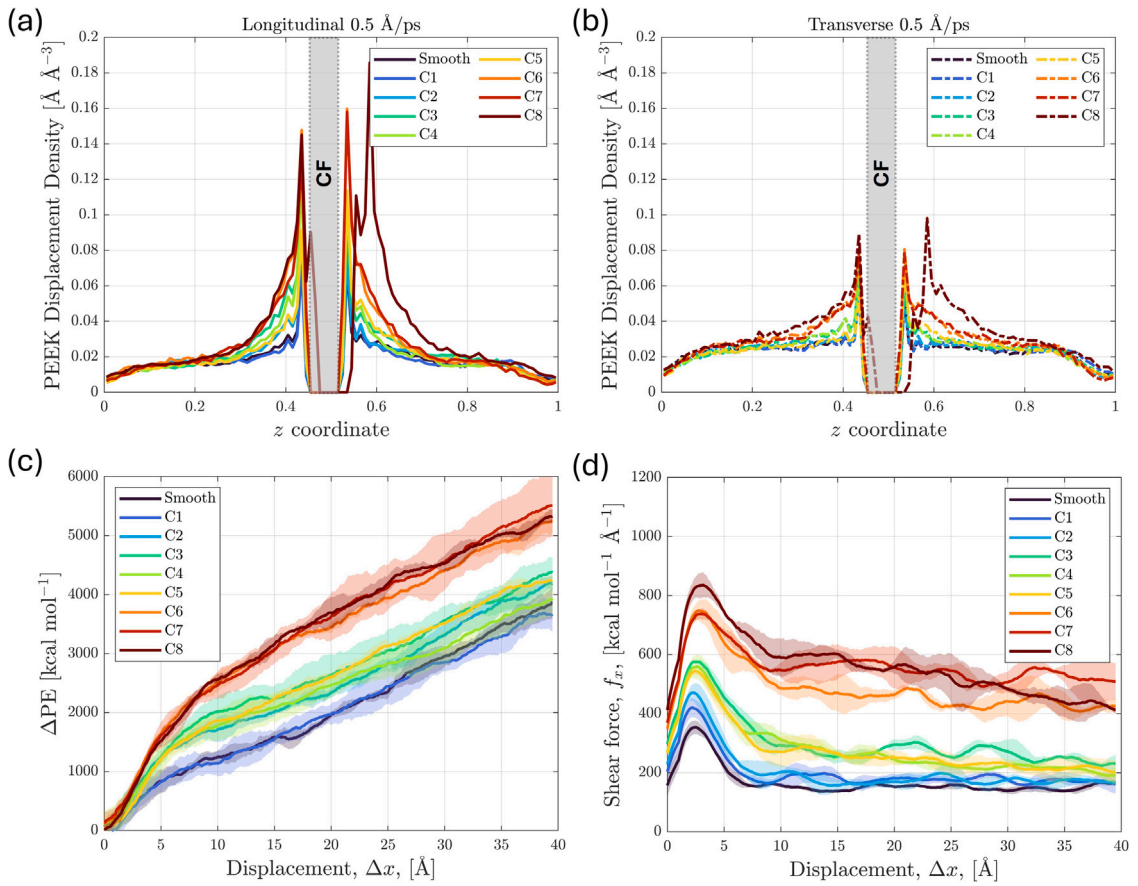


Fig. 9. Pull-out analysis at 0.5 Å ps^{-1}. PEEK displacement density along the (a) longitudinal and (b) transverse directions as a function of relative z coordinate, with the shaded region indicating the CF position. (c) Potential energy change ΔPE and (d) shear force f_x as a function of CF displacement Δx, with shaded bands representing one standard deviation across five independent realisations.

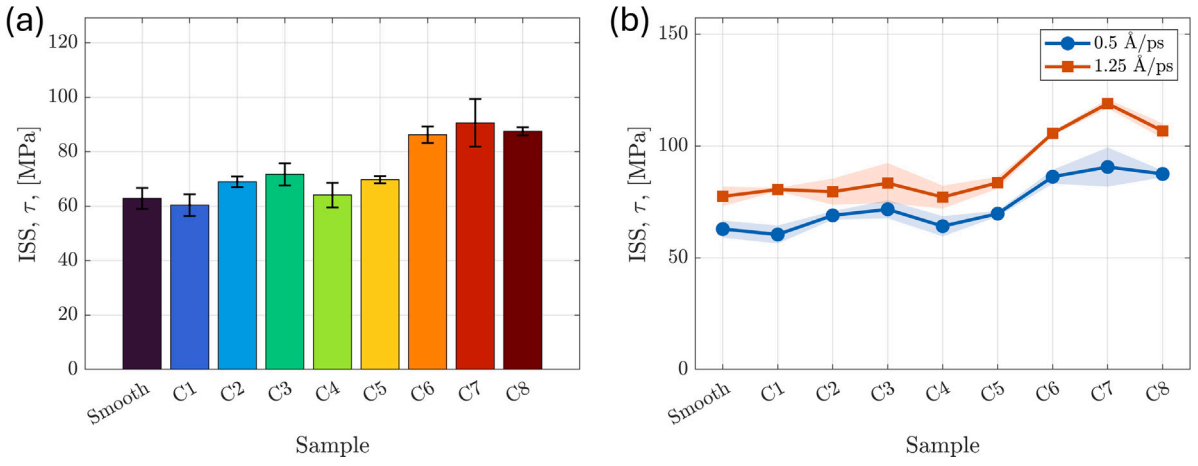


Fig. 10. ISS and interfacial structural analysis. (a) Mean ISS at 0.5 Å ps^{-1} for each configuration, with error bars representing one standard deviation. (b) ISS as a function of pull-out rate, confirming the two-regime trend is rate-independent, with shaded bands representing one standard deviation.

pooled comparison of the low-vacancy group (Smooth–C5) against the high-vacancy group (C6–C8) confirmed the separation between these two regimes ($p < 0.001$). The individual ISS values plotted against the total vacancy fraction, ϕ_{vac}, are provided in Figure S2 in the Supporting Information, highlighting the low-vacancy plateau and the transition to the higher-ISS regime at the clustered high-vacancy configurations.

Notably, C7 attained the highest ISS of all configurations despite having the lowest IE (Fig. 8(b)) and the highest vacancy fraction (ϕ_{vac} = 28.8%). This apparent contradiction highlights that static interfacial adhesion and dynamic pull-out resistance are very distinct mechanisms: IE is dominated by the available π-conjugated contact area, which is minimised by the single large open void present in C7, whereas ISS is dominated by mechanical interlocking, which the same geometry maximises by allowing PEEK chains to fully penetrate the CF plane. This decoupling between IE and ISS is consistent with prior simulation studies showing that interaction energy is not always correlated with frictional forces [22,26,37]. In the cases of C6 and C8, the vacancies are distributed as smaller stepped or layered clusters

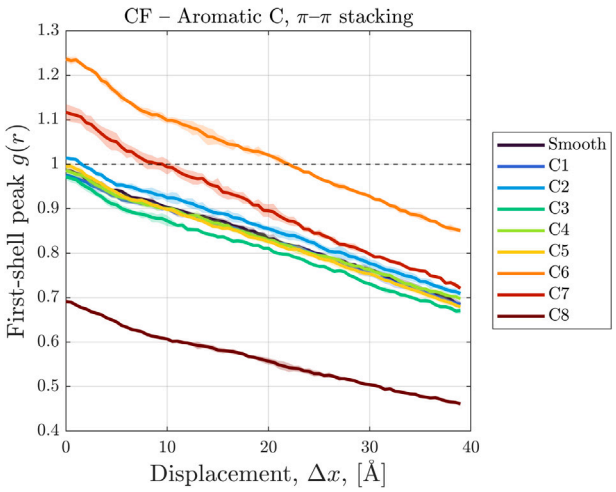


Fig. 11. Evolution of the first-shell π-π stacking peak $g(r)$ between carbon atoms and PEEK aromatic carbon as a function of CF displacement Δx during pull-out at 0.5 Å ps^{-1} (shaded bands representing one standard deviation).

(and, in the latter case, across five graphene layers; Table 1), and thus they retain more contact area and hence higher IE, while still providing sufficient anchoring points to produce a significant ISS gain. Furthermore, pairwise comparisons showed that C6, C7 and C8 were not statistically significantly different from one another, despite their different total vacancy fractions (20.2–28.8%), interaction energies, and graphene interlayer stacking arrangements (Tables S10 and S11). This suggests that the transition to the higher-ISS regime is not determined by total vacancy fraction alone but may instead depend on the spatial connectivity and morphology of the vacancy clusters, which facilitate sustained PEEK chain anchoring and mechanical interlocking.

Pull-out simulations repeated at 1.25 Å ps^{-1} (Fig. 10(b)) reproduced the same qualitative trend: a plateau across Smooth–C5 followed by a step increase at C6–C8, confirming the effect is not an artefact of the pull-out rate. The absolute ISS increased by approximately 22.7% on average across all configurations relative to 0.5 Å ps^{-1}, consistent with reduced chain relaxation time at the higher rate. Importantly, the relative vacancy-induced enhancement was retained, with C6–C8 exhibiting ISS values approximately 37–44% above the smooth reference at 0.5 Å ps^{-1} and 32–48% above the smooth reference at 1.25 Å ps^{-1} (Table S9). The C6–C8 configurations differed significantly from the smooth reference at both pull-out rates, whereas C1–C5 showed no statistically significant differences. The structural response of the PEEK matrix at both pull rates is further illustrated by sliced system visualisations (Figure S3) and longitudinal and transverse PEEK displacement density profiles provided in the Supplementary Information (Figure S4 and S5). In both cases, the same two-regime behaviour is evident: C1–C5 show narrow interfacial peaks comparable to the smooth baseline, while C6–C8 exhibit substantially broader and taller peaks, confirming that the interlocking mechanism persists at the higher pull rate. The higher pull rate suppresses absolute peak heights relative to 0.5 Å ps^{-1}, consistent with less time for PEEK chain reorganisation during displacement.

The fibre-matrix interphase was further characterised by computing the radial distribution function (RDF) between the graphene carbon atoms and each PEEK atom type (Figure S6). The evolution of π-π stacking during pull-out was tracked by computing the first-shell peak of the RDF between carbon atoms and PEEK aromatic carbon atoms as a function of graphene displacement (Fig. 11). All configurations exhibit a declining trend as graphene separates from the PEEK matrix, consistent with a progressive loss of aromatic contact. However, two distinct regimes are apparent: Smooth and C1–C5 begin near or just below $g(r) = 1$ and decline steadily to approximately 0.7 by 40 Å, whereas C6 and C7 begin significantly above $g(r) = 1$ (1.24 and 1.11, respectively) and maintain elevated stacking throughout pull-out, consistent with PEEK aromatic rings remaining in close proximity to graphene edges within the vacancy regions as the sheet translates. C8 is a notable outlier, beginning below the smooth baseline at $g(r) \approx 0.69$ and declining to 0.46 by 40 Å, a trend attributed to the five-layer geometry, which displaces PEEK chains farther from the outermost graphene surface. It should be noted that introducing a vacuum region for the CF during pull-out alters the effective simulation cell density, thereby suppressing absolute $g(r)$ values relative to a standard equilibrium RDF; the trends between configurations should therefore be interpreted in relative terms.

Taken together, the ISS and RDF analyses indicate that the interlocking-driven ISS enhancement observed for C6–C8 is accompanied by, and consistent with, sustained aromatic contact between PEEK and the CF edges within the vacancy network. Since PEEK is semi-crystalline in practical CF/PEEK composites, crystallinity may influence this interfacial behaviour by altering polymer-chain mobility and rearrangement, which could affect chain anchoring and sustained contact within the vacancy network [35]. Crystalline regions may also alter local matrix stiffness and, consequently, the extent of stress transfer across the interface [53]. The present results therefore describe the interfacial behaviour of an amorphous PEEK matrix. Tensile characterisation of the composite specimens themselves was outside the scope of the present study.

The vacancy fractions explored here are not calibrated against a measured defect density for IM7-GP fibre. AFM, the technique used to characterise roughness in this work (Fig. 6), resolves out-of-plane topography rather than in-plane atomic vacancies. Both the single-sheet defect thresholds (P1–P7) and the composite stacking configurations (C1–C8) were instead chosen to bracket a physically plausible range of disorder, from sparse, isolated defects through to a near-percolating regime, allowing the sensitivity of graphene mechanical properties and interfacial shear stress to vacancy morphology to be assessed systematically. Direct incorporation of an experimentally measured surface profile into an atomistic MD cell is constrained by the substantial scale disparity between the experimental surface and computational cell. Previous modelling work has addressed this challenge by decomposing AFM-measured carbon-fibre topography into representative asperities using Fourier analysis [31]. The framework could nevertheless be extended by applying the Perlin noise field in the z-direction to introduce correlated height variation and better represent AFM-measured surface roughness, complementing existing approaches based on reactive annealing [24] and prescribed roughness [43]. Coupling such an extended, topographically-resolved model with the present vacancy description into a single, jointly validated surface model, for example via STM or high-resolution TEM of the same fibre batch, offers a promising route to refine this framework further.

The Perlin-noise framework shares with reactive-annealing approaches the ability to generate spatially heterogeneous carbon surfaces beyond idealised graphene but introduces this complexity through spatially correlated stochastic vacancy distributions. Unlike previous non-reactive models based on prescribed geometric defects or systematic vacancy-density variation [26–30], the present approach provides control over vacancy clustering and connectivity, producing a more randomised representation of atomic-scale surface disorder. Reactive annealing instead generates surface complexity through carbon–carbon bond rearrangement and emergent topological and topographical features, including non-hexagonal carbon rings, edges, holes, and convergent sheet boundaries, as reported by Vuković and Walsh [24]. Additionally, Stone–Wales defects could be incorporated to represent a distinct class of surface disorder observed on real carbon fibre surfaces [79,80]. A further extension would be the inclusion of tailored fibre surface chemistry, *e.g.* through extended grafted groups, which can significantly enhance IFSS experimentally but whose molecular-level interactions with PEEK at defective surfaces remain poorly understood. The model developed here provides a platform for investigating these effects.

5. Conclusion

The results of the molecular dynamics modelling of a representative molecular structure of the carbon/PEEK interphase indicate:

- The PEEK matrix model was validated against empirical DSC measurements, reproducing the experimental glass transition temperature, and SEM/HS-AFM characterisation confirmed that even nominally smooth IM7-GP fibres possess coherent nanoscale roughness, supporting the case for defect-informed rather than idealised CF surface models.
- A stochastic, Perlin-noise-based defect-generation framework produces spatially correlated vacancy defects on graphene sheets compatible with standard fixed-topology force fields, offering an efficient alternative to reactive-potential annealing for generating representative CF surface surrogates.
- Vacancy defects degrade the in-plane elastic properties of graphene monotonically, with Young's and shear moduli falling by over 80% between the pristine sheet and the highest defect threshold (P7).
- Interfacial shear stress (ISS) does not follow a uniform trend: configurations with low-to-moderate vacancy fractions ($\lesssim$8%) are statistically indistinguishable from the pristine interphase, while large, spatially connected vacancy clusters (20–29%) produce a significant 37–44% ISS increase.
- This ISS enhancement is decoupled from interfacial interaction energy, indicating that mechanical interlocking of PEEK chains within the vacancy network, rather than retained π-conjugated contact area, dominates pull-out resistance at high defect densities.
- RDF analysis of π-π stacking during pull-out shows the ISS enhancement sustains elevated aromatic stacking with graphene edges throughout displacement, unlike the smooth and low-defect configurations.
- The vacancy-induced ISS increase is independent of pull-out rate, reproducing the same two-regime behaviour at both 0.5 and 1.25 Å ps^{-1}.

The framework developed here is transferable beyond the CF/PEEK system studied. Because defect level, sheet size, and stacking sequence are specified as simple input parameters, the same approach could be extended to temperature-dependent studies of interfacial property evolution or used to rapidly screen candidate surface morphologies ahead of costly experimental fibre treatments. This combination of stochastic realism and computational efficiency positions MD as a practical route for iterating on CFRP composites before committing to full experimental validation.

CRediT authorship contribution statement

Jula C. Schroeder: Writing – review & editing, Writing – original draft, Visualization, Software, Methodology, Investigation, Formal analysis, Data curation, Conceptualization. **Jonathan Meegan:** Writing – review & editing, Supervision, Resources, Project administration, Conceptualization. **Sebastien Rochat:** Writing – review & editing, Supervision, Conceptualization. **J. Patrick A. Fairclough:** Writing – review & editing, Supervision, Conceptualization. **Fabrizio Scarpa:** Writing – review & editing, Supervision, Project administration, Funding acquisition, Conceptualization. **Ian Hamerton:** Writing – review & editing, Supervision, Resources, Project administration, Funding acquisition, Conceptualization.

Declaration of competing interest

The authors declare that they have no known competing financial interests or personal relationships that could have appeared to influence the work reported in this paper.

Acknowledgements

This work was supported and funded by the EPSRC Centre, UK for Doctoral Training in Composites Science, Engineering, and Manufacturing (CDT CoSEM) [EP/S021728/1] at the University of Bristol. J.C.S. acknowledges the computational facilities of the Advanced Computing Research Centre, University of Bristol - http://www.bristol.ac.uk/acrc/. F. S. acknowledges the partial support from the ERC-2020-AdG 101020715 NEUROMETA project. The authors acknowledge the use of resources provided by the Isambard 3 Tier-2 HPC Facility. Isambard 3 is hosted by the University of Bristol and operated by the GW4 Alliance (https://gw4.ac.uk) and is funded by UK Research and Innovation; and the Engineering and Physical Sciences Research Council [EP/X039137/1]. The authors would like to thank the anonymous Reviewers for the constructive and useful suggestions that have helped strengthening the quality of the manuscript.

Appendix A. Supplementary data

Supplementary material related to this article can be found online at https://doi.org/10.1016/j.compscitech.2026.111885.

Data availability

The code for the graphene sheet generator is publicly available and can be downloaded from GitHub at https://github.com/JulaSchroeder/CF-Surface All other data will be made available on request.

Code for graphene sheet generator (Original data) (GitHub)

References

[1] K. Ramaswamy, V. Modi, P.S. Rao, P.P. Martin, C.T. McCarthy, R.M. O'Higgins, An investigation of the influence of matrix properties and fibre–matrix interface behaviour on the mechanical performance of carbon fibre-reinforced PEKK and PEEK composites, Compos. Part A: Appl. Sci. Manuf. 165 (2023) 107359, http://dx.doi.org/10.1016/j.compositesa.2022.107359.

[2] D. Mamalis, J.J. Murray, J. McClements, D. Tsikritsis, V. Koutsos, E.D. McCarthy, C.M. Ó Brádaigh, Novel carbon-fibre powder-epoxy composites: Interface phenomena and interlaminar fracture behaviour, Compos. Part B: Eng. 174 (2019) 107012, http://dx.doi.org/10.1016/j.compositesb.2019.107012.

[3] H. Pérez-Martín, P. Mackenzie, A. Baidak, C.M. Ó Brádaigh, D. Ray, Crystallinity studies of PEKK and carbon fibre/PEKK composites: A review, Compos. Part B: Eng. 223 (2021) 109127, http://dx.doi.org/10.1016/j.compositesb.2021.109127.

[4] B. Rohrmüller, P. Gumbsch, J. Hohe, Calibrating a fiber–matrix interface failure model to single fiber push-out tests and numerical simulations, Compos. Part A: Appl. Sci. Manuf. 150 (2021) 106607, http://dx.doi.org/10.1016/j.compositesa.2021.106607.

[5] A.J. Timmis, A. Hodzic, L. Koh, M. Bonner, C. Soutis, A.W. Schäfer, L. Dray, Environmental impact assessment of aviation emission reduction through the implementation of composite materials, Int. J. Life Cycle Assess. 20 (2) (2015) 233–243, http://dx.doi.org/10.1007/s11367-014-0824-0.

[6] G.M. Odegard, S.U. Patil, P.P. Deshpande, K. Kanhaiya, J.J. Winetrout, H. Heinz, S.P. Shah, M. Maiaru, Molecular dynamics modeling of epoxy resins using the reactive interface force field, Macromolecules 54 (21) (2021) 9815–9824, http://dx.doi.org/10.1021/acs.macromol.1c01813.

[7] H. Al Mahmud, M.S. Radue, S. Chinkanjanarot, W.A. Pisani, S. Gowtham, G.M. Odegard, Multiscale modeling of carbon fiber- graphene nanoplatelet-epoxy hybrid composites using a reactive force field, Compos. Part B: Eng. 172 (2019) 628–635, http://dx.doi.org/10.1016/j.compositesb.2019.05.035.

[8] B. Demir, K.M. Beggs, B.L. Fox, L. Servinis, L.C. Henderson, T.R. Walsh, A predictive model of interfacial interactions between functionalised carbon fibre surfaces cross-linked with epoxy resin, Compos. Sci. Technol. 159 (2018) 127–134, http://dx.doi.org/10.1016/j.compscitech.2018.02.029.

[9] B. Demir, L.C. Henderson, T.R. Walsh, Design rules for enhanced interfacial shear response in functionalized carbon fiber epoxy composites, ACS Appl. Mater. Interfaces 9 (13) (2017) 11846–11857, http://dx.doi.org/10.1021/acsami.6b16041.

[10] Q. Wu, Q. Wan, Q. Liu, J. He, R. Zhao, X. Yang, F. Wang, J. Guo, J. Zhu, Synergistic strengthening and toughening the interphase of composites by constructing alternating "rigid-and-soft" structure on carbon fiber surface, Adv. Mater. Interfaces 6 (21) (2019) 1900970, http://dx.doi.org/10.1002/admi.201900970.

[11] S. AhmadvashAghbash, I. Verpoest, Y. Swolfs, M. Mehdikhani, Methods and models for fibre–matrix interface characterisation in fibre-reinforced polymers: a review, Int. Mater. Rev. 68 (8) (2023) 1245–1319, http://dx.doi.org/10.1080/09506608.2023.2265701.

[12] X. Yuan, Z. Zhang, X. Mu, C. Shan, X. Gao, B. Zhu, Recent progress on interface characterization methods of carbon fiber reinforced polymer composites, Chem. Eng. J. 499 (2024) 156220, http://dx.doi.org/10.1016/j.cej.2024.156220.

[13] J. Sha, J. Dai, J. Li, Z. Wei, J.-M. Hausherr, W. Krenkel, Measurement and analysis of fiber-matrix interface strength of carbon fiber-reinforced phenolic resin matrix composites, J. Compos. Mater. 48 (11) (2014) 1303–1311, http://dx.doi.org/10.1177/0021998313485264.

[14] M. Sharma, S. Gao, E. Mäder, H. Sharma, L.Y. Wei, J. Bijwe, Carbon fiber surfaces and composite interphases, Compos. Sci. Technol. 102 (2014) 35–50, http://dx.doi.org/10.1016/j.compscitech.2014.07.005.

[15] D. Gaitanelis, C. Worrall, M. Kazilas, Influence of rapid high-temperature processing on the interface of CF/PEEK, a quick and effective method for enhancing the IFSS, Compos. Sci. Technol. 251 (2024) 110564, http://dx.doi.org/10.1016/j.compscitech.2024.110564.

[16] Y. Chandra, F. Scarpa, S. Adhikari, J. Zhang, E.I. Saavedra Flores, H.-X. Peng, Pullout strength of graphene and carbon nanotube/epoxy composites, Compos. Part B: Eng. 102 (2016) 1–8, http://dx.doi.org/10.1016/j.compositesb.2016.06.070.

[17] D.A. Damasceno, E. Mesquita, R.K.N.D. Rajapakse, R. Pavanello, Atomic-scale finite element modelling of mechanical behaviour of graphene nanoribbons, Int. J. Mech. Mater. Des. 15 (1) (2019) 145–157, http://dx.doi.org/10.1007/s10999-018-9403-z.

[18] K.N. Spanos, S.K. Georgantzinos, N.K. Anifantis, Mechanical properties of graphene nanocomposites: A multiscale finite element prediction, Compos. Struct. 132 (2015) 536–544, http://dx.doi.org/10.1016/j.compstruct.2015.05.078.

[19] B. Demir, T.R. Walsh, A robust and reproducible procedure for cross-linking thermoset polymers using molecular simulation, Soft Matter 12 (8) (2016) 2453–2464, http://dx.doi.org/10.1039/C5SM02788H.

[20] F. Vuković, B. Newman, Y. Yin, G.G. Andersson, L.C. Henderson, T.R. Walsh, Decoupling the effects of topographical roughness and oxidation on the interfacial properties of carbon fiber-epoxy composites, Compos. Sci. Technol. 271 (2025) 111354, http://dx.doi.org/10.1016/j.compscitech.2025.111354.

[21] Z. Song, Y. Li, B. Yang, The interfacial load-transfer enhancement mechanism of amino-functionalised carbon nanotube reinforced epoxy matrix composites: A molecular dynamics study, Compos. Sci. Technol. 209 (2021) 108790, http://dx.doi.org/10.1016/j.compscitech.2021.108790.

[22] P.P. Deshpande, M.S. Radue, P. Gaikwad, S. Bamane, S.U. Patil, W.A. Pisani, G.M. Odegard, Prediction of the interfacial properties of high-performance polymers and flattened CNT-reinforced composites using molecular dynamics, Langmuir 37 (39) (2021) 11526–11534, http://dx.doi.org/10.1021/acs.langmuir.1c01800.

[23] J. Zhu, Z. Gao, M. Kowalik, K. Joshi, C.M. Ashraf, M.I. Arefev, Y. Schwab, C. Bumgardner, K. Brown, D.E. Burden, L. Zhang, J.W. Klett, L.V. Zhigilei, A.C.T. van Duin, X. Li, Unveiling carbon ring structure formation mechanisms in polyacrylonitrile-derived carbon fibers, ACS Appl. Mater. Interfaces 11 (45) (2019) 42288–42297, http://dx.doi.org/10.1021/acsami.9b15833.

[24] F. Vuković, T.R. Walsh, Practical atomistic models of carbon fiber surfaces with tuneable topology and topography, Compos. Sci. Technol. 216 (2021) 109049, http://dx.doi.org/10.1016/j.compscitech.2021.109049.

[25] S. Desai, C. Li, T. Shen, A. Strachan, Molecular modeling of the microstructure evolution during carbon fiber processing, J. Chem. Phys. 147 (22) (2017) 224705, http://dx.doi.org/10.1063/1.5000911.

[26] S.U. Patil, J. Kemppainen, T. Wavrunek, G.M. Odegard, The effect of gamma-ray irradiation on polymer-graphene nanocomposite interfaces, Compos. Part B: Eng. 284 (2024) 111715, http://dx.doi.org/10.1016/j.compositesb.2024.111715.

[27] D. Pan, H. Wang, K. Zhu, Z. Tang, X. Hao, Molecular dynamics simulation and finite element method investigation of PTFE/carbon fiber composite tribological properties, Tribol. Int. 180 (2023) 108241, http://dx.doi.org/10.1016/j.triboint.2023.108241.

[28] J.P. Johnston, B. Koo, N. Subramanian, A. Chattopadhyay, Modeling the molecular structure of the carbon fiber/polymer interphase for multiscale analysis of composites, Compos. Part B: Eng. 111 (2017) 27–36, http://dx.doi.org/10.1016/j.compositesb.2016.12.008.

[29] P. Yang, W. Kong, B. Li, S. Liang, Y. Qu, P. Shi, G. Li, X. Yang, Enhanced thermal conductive and interfacial performance of M40X carbon fiber/epoxy composites with multi-dimensional liquid crystalline interphase: A combined method of experimental analysis and molecular simulation, Compos. Part B: Eng. 307 (2025) 112866, http://dx.doi.org/10.1016/j.compositesb.2025.112866.

[30] J. Zhang, J. Han, L. Wu, L. Chen, Q. Jiang, Data-driven analysis of heterogeneity effects on carbon fiber/epoxy interfaces using molecular dynamics and machine learning, Compos. Part B: Eng. 319 (2026) 113667, http://dx.doi.org/10.1016/j.compositesb.2026.113667.

[31] T. Sohail, S. Nakarmi, R. Sweat, R. Baughman, H. Lu, S. Roy, Simulation of surface asperities on a carbon fiber using molecular dynamics and fourier series decomposition to predict interfacial shear strength in polymer matrix composites, Compos. Interfaces 29 (8) (2022) 947–970, http://dx.doi.org/10.1080/09276440.2022.2029314.

[32] N.A. Garcia, J.B. Awuah, C. Zhao, F. Vuković, T.R. Walsh, Simulation-ready graphene oxide structures with hierarchical complexity: a modular tiling strategy, in: 2D Materials, Vol. 10, IOP Publishing, 2023, 025007, http://dx.doi.org/10.1088/2053-1583/acb0e1.

[33] H. Lyu, N. Jiang, Y. Li, H. Lee, D. Zhang, Enhanced interfacial and mechanical properties of carbon fiber/PEEK composites by hydroxylated PEEK and carbon nanotubes, Compos. Part A: Appl. Sci. Manuf. 145 (2021) 106364, http://dx.doi.org/10.1016/j.compositesa.2021.106364.

[34] H. Liu, Y. Zhao, N. Li, X. Zhao, X. Han, S. Li, W. Lu, K. Wang, S. Du, Enhanced interfacial strength of carbon fiber/PEEK composites using a facile approach via PEI&ZIF-67 synergistic modification, J. Mater. Res. Technol. 8 (6) (2019) 6289–6300, http://dx.doi.org/10.1016/j.jmrt.2019.10.022.

[35] E.A.M. Hassan, L. Yang, T.H.H. Elagib, D. Ge, X. Lv, J. Zhou, M. Yu, S. Zhu, Synergistic effect of hydrogen bonding and π-π stacking in interface of CF/PEEK composites, Compos. Part B: Eng. 171 (2019) 70–77, http://dx.doi.org/10.1016/j.compositesb.2019.04.015.

[36] P. Xu, Y. Yu, Z. Guo, X. Zhang, G. Li, X. Yang, Evaluation of composite interfacial properties based on carbon fiber surface chemistry and topography: Nanometer-scale wetting analysis using molecular dynamics simulation, Compos. Sci. Technol. 171 (2019) 252–260, http://dx.doi.org/10.1016/j.compscitech.2018.12.028.

[37] W.A. Pisani, M.S. Radue, S.U. Patil, G.M. Odegard, Interfacial modeling of flattened CNT composites with cyanate ester and PEEK polymers, Compos. Part B: Eng. 211 (2021) 108672, http://dx.doi.org/10.1016/j.compositesb.2021.108672.

[38] Q.N. Hoang, S. Lee, S. Lee, H. Park, Characterization of CFRP interface properties with varying fiber surface roughness using AFM measurements and finite element modeling, Compos. Part B: Eng. 308 (2026) 112990, http://dx.doi.org/10.1016/j.compositesb.2025.112990.

[39] K. Perlin, An image synthesizer, ACM SIGGRAPH Comput. Graph. 19 (3) (1985) 287–296, http://dx.doi.org/10.1145/325165.325247.

[40] M. Bennett, Frequency spectra filtering for Perlin noise, Comput. Games J. 8 (1) (2019) 13–24, http://dx.doi.org/10.1007/s40869-018-0074-7.

[41] R.M. Smelik, T. Tutenel, R. Bidarra, B. Benes, A survey on procedural modelling for virtual worlds, Comput. Graph. Forum 33 (6) (2014) 31–50, http://dx.doi.org/10.1111/cgf.12276.

[42] D. Feng, Multi-scale algorithm for controllable virtual aggregate generation in mesoscale modeling, Int. J. Mech. Sci. 308 (2025) 110978, http://dx.doi.org/10.1016/j.ijmecsci.2025.110978.

[43] I. Georgakopoulos-Soares, E.L. Papazoglou, A.P. Markopoulos, On the use of the Perlin noise function to calculate the laser absorption coefficient by rough surfaces, Simul. Model. Pract. Theory 124 (2023) 102722, http://dx.doi.org/10.1016/j.simpat.2022.102722.

[44] A.P. Thompson, H.M. Aktulga, R. Berger, D.S. Bolintineanu, W.M. Brown, P.S. Crozier, P.J. in 't Veld, A. Kohlmeyer, S.G. Moore, T.D. Nguyen, R. Shan, M.J. Stevens, J. Tranchida, C. Trott, S.J. Plimpton, LAMMPS - a flexible simulation tool for particle-based materials modeling at the atomic, meso, and continuum scales, Comput. Phys. Comm. 271 (2022) 108171, http://dx.doi.org/10.1016/j.cpc.2021.108171.

[45] P.J. in 't Veld, G.C. Rutledge, Temperature-dependent elasticity of a semicrystalline interphase composed of freely rotating chains, Macromolecules 36 (19) (2003) 7358–7365, http://dx.doi.org/10.1021/ma0346658.

[46] H. Sun, S.J. Mumby, J.R. Maple, A.T. Hagler, An ab initio CFF93 all-atom force field for polycarbonates, J. Am. Chem. Soc. 116 (7) (1994) 2978–2987, http://dx.doi.org/10.1021/ja00086a030.

[47] I. Yungerman, I. Starodumov, A. Fulati, K. Uto, M. Ebara, Y. Moskovitz, Full-atomistic optimized potentials for liquid simulations and polymer consistent force field models for biocompatible shape-memory poly(ϵ-caprolactone), J. Phys. Chem. B 126 (21) (2022) 3961–3972, http://dx.doi.org/10.1021/acs.jpcb.2c01973.

[48] O.V. Kashurin, N.D. Kondratyuk, A.V. Lankin, G.E. Norman, Force field comparison for molecular dynamics simulations of liquid membranes, J. Mol. Liq. 416 (2024) 126347, http://dx.doi.org/10.1016/j.molliq.2024.126347.

[49] A.N. Rissanou, A.J. Power, V. Harmandaris, Structural and dynamical properties of polyethylene/graphene nanocomposites through molecular dynamics simulations, Polymers 7 (3) (2015) 390–417, http://dx.doi.org/10.3390/polym7030390.

[50] W.G. Hoover, Canonical dynamics: Equilibrium phase-space distributions, Phys. Rev. A 31 (3) (1985) 1695–1697, http://dx.doi.org/10.1103/PhysRevA.31.1695.

[51] S. Nosé, A molecular dynamics method for simulations in the canonical ensemble, Mol. Phys. 52 (2) (1984) 255–268, http://dx.doi.org/10.1080/00268978400101201.

[52] A. Stukowski, Visualization and analysis of atomistic simulation data with OVITO–the open visualization tool, Modelling Simul. Mater. Sci. Eng. 18 (1) (2009) 015012, http://dx.doi.org/10.1088/0965-0393/18/1/015012.

[53] K. Kashmari, H. Al Mahmud, S.U. Patil, W.A. Pisani, P. Deshpande, M. Maiaru, G.M. Odegard, Multiscale process modeling of semicrystalline PEEK for tailored thermomechanical properties, ACS Appl. Eng. Mater. 1 (11) (2023) 3167–3177, http://dx.doi.org/10.1021/acsaenm.3c00586.

[54] D. Sheppard, R. Terrell, G. Henkelman, Optimization methods for finding minimum energy paths, J. Chem. Phys. 128 (13) (2008) 134106, http://dx.doi.org/10.1063/1.2841941.

[55] A. Brünger, C.L. Brooks, M. Karplus, Stochastic boundary conditions for molecular dynamics simulations of ST2 water, Chem. Phys. Lett. 105 (5) (1984) 495–500, http://dx.doi.org/10.1016/0009-2614(84)80098-6.

[56] S.J. Stuart, A.B. Tutein, J.A. Harrison, A reactive potential for hydrocarbons with intermolecular interactions, J. Chem. Phys. 112 (14) (2000) 6472–6486, http://dx.doi.org/10.1063/1.481208.

[57] M.A. Torkaman-Asadi, M.A. Kouchakzadeh, Atomistic simulations of mechanical properties and fracture of graphene: A review, Comput. Mater. Sci. 210 (2022) 111457, http://dx.doi.org/10.1016/j.commatsci.2022.111457.

[58] T. Ramanathan, A.A. Abdala, S. Stankovich, D.A. Dikin, M. Herrera-Alonso, R.D. Piner, D.H. Adamson, H.C. Schniepp, X. Chen, R.S. Ruoff, S.T. Nguyen, I.A. Aksay, R.K. Prud'Homme, L.C. Brinson, Functionalized graphene sheets for polymer nanocomposites, Nature Nanotechnology 3 (6) (2008) 327–331, http://dx.doi.org/10.1038/nnano.2008.96.

[59] S. He, T.R. Walsh, Prediction of chain-growth polymerisation of vinyl ester resin structure at the carbon fibre interface, Compos. Sci. Technol. 218 (2022) 109168, http://dx.doi.org/10.1016/j.compscitech.2021.109168.

[60] D. Nečas, P. Klapetek, Gwyddion: an open-source software for SPM data analysis, Open Phys. 10 (1) (2012) 181–188, http://dx.doi.org/10.2478/s11534-011-0096-2.

[61] C.L. Choy, W.P. Leung, C. Nakafuku, Thermal expansion of poly(ether-ether-ketone) (PEEK), J. Polym. Sci. Part B: Polym. Phys. 28 (11) (1990) 1965–1977, http://dx.doi.org/10.1002/polb.1990.090281107.

[62] G.M. Odegard, S.U. Patil, P.S. Gaikwad, P. Deshpande, A.S. Krieg, S.P. Shah, A. Reyes, T. Dickens, J.A. King, M. Maiaru, Accurate predictions of thermoset resin glass transition temperatures from all-atom molecular dynamics simulation, Soft Matter 18 (39) (2022) 7550–7558, http://dx.doi.org/10.1039/D2SM00851C.

[63] P.S. Gaikwad, A.S. Krieg, P.P. Deshpande, S.U. Patil, J.A. King, M. Maiaru, G.M. Odegard, Understanding the origin of the low cure shrinkage of polybenzoxazine resin by computational simulation, ACS Appl. Polym. Mater. 3 (12) (2021) 6407–6415, http://dx.doi.org/10.1021/acsapm.1c01164.

[64] K. Rothe, N. Néel, J. Kröger, Unveiling the nature of atomic defects in graphene on a metal surface, Beilstein J. Nanotechnol. 15 (2024) 416–425, http://dx.doi.org/10.3762/bjnano.15.37.

[65] M. Datt Bhatt, H. Kim, G. Kim, Various defects in graphene: a review, RSC Adv. 12 (33) (2022) 21520–21547, http://dx.doi.org/10.1039/D2RA01436J.

[66] A. Jafari, K. Aliakbari, M. Amiri, S. Rouhi, Characterization of mechanical properties of graphene nanoplates with vacancy defects using AFEM, Sci. Rep. 15 (1) (2025) 24148, http://dx.doi.org/10.1038/s41598-025-07241-w.

[67] C. Lee, X. Wei, J.W. Kysar, J. Hone, Measurement of the elastic properties and intrinsic strength of monolayer graphene, Science 321 (5887) (2008) 385–388, http://dx.doi.org/10.1126/science.1157996.

[68] X. Liu, T.H. Metcalf, J.T. Robinson, B.H. Houston, F. Scarpa, Shear modulus of monolayer graphene prepared by chemical vapor deposition, Nano Lett. 12 (2) (2012) 1013–1017, http://dx.doi.org/10.1021/nl204196v.

[69] S. Thomas, K. M. Ajith, S. Uck Lee, M. C. Valsakumar, Assessment of the mechanical properties of monolayer graphene using the energy and strain-fluctuation methods, RSC Adv. 8 (48) (2018) 27283–27292, http://dx.doi.org/10.1039/C8RA02967A.

[70] J. Stratmann, B. Markert, F. Bamer, Numerical investigation of the Poisson's ratio of amorphous graphene sheets, Proc. Appl. Math. Mech. 23 (4) (2023) e202300243, http://dx.doi.org/10.1002/pamm.202300243.

[71] H. Uematsu, T. Aratama, K. Sudo, Y. Ito, A. Yamaguchi, A. Fukushima, S. Sugihara, F. Nishimura, M. Yamane, S. Tanoue, Antioxidant-enhanced interfacial adhesion and mechanical properties of polyetheretherketone–carbon fiber composites, Polymer 328 (2025) 128415, http://dx.doi.org/10.1016/j.polymer.2025.128415.

[72] S. Lamorinière, M.P. Jones, K. Ho, G. Kalinka, M.S.P. Shaffer, A. Bismarck, Carbon nanotube enhanced carbon fibre-poly(ether ether ketone) interfaces in model hierarchical composites, Compos. Sci. Technol. 221 (2022) 109327, http://dx.doi.org/10.1016/j.compscitech.2022.109327.

[73] N. Li, J. Chen, H. Liu, A. Dong, K. Wang, Y. Zhao, Effect of preheat treatment on carbon fiber surface properties and fiber/PEEK interfacial behavior, Polym. Compos. 40 (S2) (2019) E1407–E1415, http://dx.doi.org/10.1002/pc.25020.

[74] M.T. Umemura, F. Dalmas, P. Reynaud, D. Long, G. Fantozzi, N. Godin, L. Trouillet-Fonti, J. Bikard, Fiber-matrix interface characterization in CF/PEEK composites by analysis of single fiber fragmentation, Compos. Sci. Technol. 270 (2025) 111301, http://dx.doi.org/10.1016/j.compscitech.2025.111301.

[75] L. Chai, B. Zhang, L. Qiao, P. Wang, L. Weng, Influence of gamma irradiation-induced surface oxidation on tribological property of polyetheretherketone (PEEK), Polym. Bull. 79 (8) (2022) 6513–6531, http://dx.doi.org/10.1007/s00289-021-03825-4.

[76] K.M. Beggs, J.D. Randall, L. Servinis, A. Krajewski, R. Denning, L.C. Henderson, Increasing the resistivity and IFSS of unsized carbon fibre by covalent surface modification, React. Funct. Polym. 129 (2018) 123–128, http://dx.doi.org/10.1016/j.reactfunctpolym.2017.06.016.

[77] S. Tiwari, J. Bijwe, S. Panier, Gamma radiation treatment of carbon fabric to improve the fiber–matrix adhesion and tribo-performance of composites, Wear 271 (9) (2011) 2184–2192, http://dx.doi.org/10.1016/j.wear.2010.11.032.

[78] J.G. Park, C. Evers, C. Jolowsky, B. Vondrasek, K. Thagard, M. Czabaj, B. Ku, Y. Wang, T. Dumitrică, G.M. Odegard, Z. Liang, Gamma-ray irradiation to achieve high tensile performance of unidirectional CNT yarn laminates, Carbon 216 (2024) 118530, http://dx.doi.org/10.1016/j.carbon.2023.118530.

[79] J. Moon, S. Yang, M. Cho, Interfacial strengthening between graphene and polymer through Stone-Thrower-Wales defects: *ab initio* and molecular dynamics simulations, Carbon 118 (2017) 66–77, http://dx.doi.org/10.1016/j.carbon.2017.03.021.

[80] Y. Li, B. Yang, Z. Yu, S. Wang, Q. Wang, A study on effects of stone–thrower–wales defective carbon nanotubes on glass transition temperature of polymer composites using molecular dynamics simulations, Comput. Mater. Sci. 186 (2021) 110005, http://dx.doi.org/10.1016/j.commatsci.2020.110005.